JSST
Journal of Space Science and Technology

P-ISSN: 2008-4560
E-ISSN: 2423-4516

Journal of Space Science and Technology

Vol. 17, Special Issue, pp. 32-44, 2024
https://doi.org/10.22034/jsst.2024.1497
Journal Homepage: https://jsstpub.com

Original Research Paper

Detailed Algorithm for Implementing Circle Criterion in QFT Framework for Saturation Nonlinearity

Hamed Kashani*

Aerospace Research Institute, Ministry of Science, Research and Technology, Tehran, Iran

ARTICLE INFO

Article History:

Received 17 August 2024
Revised 22 September 2024
Accepted 06 October 2024
Available Online 19 October 2024

Keywords:

Robust control
Quantitative feedback theory saturation
Non-interfering architecture
Circle criterion

ABSTRACT

Controlling a spacecraft's orbit and attitude is one of the most complicated problems in control engineering. Engineers encounter uncertainty and nonlinearity due to large flexible appendages and saturated electromechanical or electrohydraulic actuators. Control design methods for dealing with such problems may involve many calculations. Matlab software automates many design methods in its control system toolbox, providing algorithms for systematically analyzing, designing, and tuning linear control systems. Many other advanced design methods must also be automated to achieve fast and accurate controller design for more complex control systems. As a sample, plant uncertainty, prevalent in space systems, requires robust consideration in the design process. Quantitative feedback theory (QFT), as a powerful method for addressing such complex issues, requires plenty of calculations that make it necessary for the method to be automated. A QFT design toolbox is developed by Tersoft company. However, this toolbox cannot treat some practical issues, such as actuator saturation in its design process. In the QFT framework, saturation can be dealt with by Horowitz architecture or noninterfering loop architecture, containing an inner loop around the saturation element in the control loop. The circle criterion is a critical constraint on the inner loop transfer function, ensuring stability. This paper presents a comprehensive algorithm for automating the process of obtaining inner loop compensator design constraints, with detailed flowcharts to facilitate software development. To verify the proposed algorithm, the boundary on the saturation loop compensator, H(s), for a hydraulic actuator is determined using computer codes implemented in the Matlab environment. Intermediate and final results are presented to follow the calculations step by step up. Finally, the validity of this boundary is checked by placing its points into the circle criterion's mathematical expression and observing if the resultant points fall outside the reference circle.

*Corresponding Author's E-mail: kashani@ari.ac.ir

How to Cite this Article:
H. Kashani, "Detailed algorithm for implementing circle criterion in QFT framework for saturation nonlinearity," *Journal of Space Science and Technology*, Vol. 17, Special Issue, pp. 32-44, 2024, https://doi.org/10.22034/jsst.2024.1497.

NOMENCLATURE

SYMBOL	DESCRIPTION
μ_1	Lower Limit Of Sector Nonlinearity
μ_2	Upper Limit Of Sector Nonlinearity
C	Plant Output
F	Prefilter Transfer Function
G	Loop Shaping Transfer Function
H	Inner Loop Compensator Transfer Function
$\mathcal{I}_C$	Imaginary Part Of Complex Number C
P	Plant Transfer Function
R	Reference Input
$\mathcal{R}_C$	Real Part Of Complex Number C
X	Input Of Saturation Element
Y	Output Of Saturation Element, Plant Input

1. INTRODUCTION

Aerospace systems are the most complex with various plant and environment nonlinearity and uncertainty complexities. Attitude and orbit control systems for uncertain plants, such as space systems with large flexible structures or their components such as nonlinear actuators, pose a quite challenging design problem in the presence of nonlinearities like actuator saturation [1-3].

One of the most powerful robust control design methods in the presence of plant uncertainty or nonlinearity is Quantitative Feedback Theory (QFT). At each frequency of interest, QFT imposes a boundary on the transfer function of the loop shaper, $G(s)$ [4]. However, in most practical problems, designing the transfer function $G(s)$ to shape the loop and determining the prefilter $F(s)$ to limit the system's frequency response within a desired boundary are not the final stages of the design process. Various practical issues, such as plant input saturation, can lead to instability and performance degradation. To address the absolute stability problem arising from saturation, the noninterfering architecture proposed in [5] can be employed. The circle criterion proves the absolute stability of this architecture.

As the stability and performance requirements impose boundaries on $G(s)$ in the first stage of design, the circle criterion determines some boundaries for $H(s)$ in the second stage of the design. Extracting the boundaries above from requirements typically involves a significant amount of calculations. Once the boundaries are determined, designing compensators that satisfy these boundaries also requires substantial effort.

The Matlab software automates many classical control design methods [6]. Terasoft company has developed a QFT toolbox that automates the boundary calculation in the first design step [7]. Furthermore, [8] proposes a method to automate compensator synthesis in the first design stage. This paper contributes to developing an algorithm for automating the calculation of absolute stability boundaries in the second design stage for saturating plant input.

In the next section, we briefly describe the suitable architecture within the QFT framework for addressing saturation in the loop. Ensuring stability under saturation using the circle criterion is introduced in section 3. The main contribution of this article is presented in section 4, which describes the algorithm for implementing the circle criterion in the QFT framework. In section 5, an illustrative example is used to examine the validity of the proposed algorithm. Finally, concluding remarks are presented in the last section of the paper.

2. LOOP ARCHITECTURE FOR TREATING SATURATION

The QFT framework has two main architectures for treating saturation to achieve the desired stability and performance. The first is based on Horowitz's opinion, which affects the design of $G(s)$ [9]. Another approach can be used to simplify the design process, consisting of two steps. In the first step, two controllers, $G(s)$ and $F(s)$, are designed using a common QFT design procedure, ignoring the saturation. In the second step, controller $H(s)$ is designed to reduce the undesired effects of plant input saturation. Fig. 1 shows this noninterfering architecture for addressing saturation in the plant input [10]. The term "noninterfering" is used because the compensator $H(s)$ is not active until the plant input saturates. According to this architecture, the loop transmission around the saturation element L_n can be written as follows.

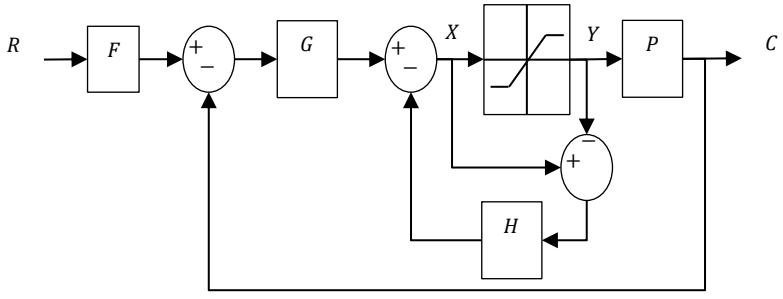

Fig. 1. Noninterfering control architecture [5].

$$L_n = -\frac{X}{Y} = \frac{L-H}{1+H} \quad (1)$$

Where, $L = GP$.

To ensure stability and achieve desired performance $H(s)$ must satisfy certain constraints [5]. In this article, only the circle criterion, a constraint associated with stability, is considered. The next section briefly explains the circle criterion, and readers can refer to reference [11] for more details.

2.1 Applying the Circle Criterion

In the scalar case, the circle criterion for a sector nonlinearity $N \in [\mu_1, \mu_2]$ with $\mu_2 > \mu_1$ states that the system presented in Fig. 1 is absolutely stable if the transfer function

$$Z(s) = \frac{1+\mu_2 L_n(s)}{1+\mu_1 L_n(s)} \quad (2)$$

is strictly positive real [11]. Strictly positive realness, at first, requires it is not identically zero. $Z(s)$ is identically zero if and only if $L_n(s) = -1/\mu_2$. This is a highly unusual scenario in practice because L_n is dynamic and depends on frequency. The second condition is that $Z(s)$ must be Hurwitz, and the third condition is expressed by Eq. (3).

$$\mathrm{Re}\left[\frac{1+\mu_2 L_n(j\omega)}{1+\mu_1 L_n(j\omega)}\right] > 0, \forall\omega \in \mathbb{R} \quad (3)$$

Now, there are three different cases depending on the sign of μ_1:

a) $0 < \mu_1 < \mu_2$,

b) $0 = \mu_1 < \mu_2$ and

c) $\mu_1 < 0 < \mu_2$.

In practice, saturation nonlinearity is typically categorized in case a, with the specific condition of $0 < \mu_1 < 1$. In this case, the third condition can be expressed as Eq. (4).

$$\mathrm{Re}\left[\frac{1+L_n(j\omega)}{\frac{1}{\mu_1}+L_n(j\omega)}\right] > 0, \forall\omega \in \mathbb{R} \quad (4)$$

Inequality (4) is equivalent to inequality (5), which can be proven by expressing $L_n = Re[L_n] + iIm[L_n]$ in inequality (4), simplifying the result, splitting the term $1/\mu_1 = 1/2\mu_1 + 1/2\mu_1$. By moving one of these terms to the right-hand side of the inequality, adding the term $(1/\mu_1^2 + 1)/4$ and finally, simplifying both sides of inequality leads to the following form of constraint.

$$\left|L_n(j\omega) + \frac{1/\mu_1 + 1}{2}\right| > \frac{1/\mu_1 - 1}{2} \quad (5)$$

Fig. 2 depicts the graphical representation of inequality (5) in the Nyquist plane and illustrates that the circle criterion necessitates that L_n does not penetrate region D. In this figure, the vectors r_1 and r_2 are equal to $1/\mu_1 + L_n\,(j\omega)$ and $1 + L_n(j\omega)$, respectively.

Although local absolute stability is guaranteed under $H(s)$ with circle criterion satisfaction, it is still possible for limit cycles to occur, especially when the plant has a high type (i.e., $n \geq 3$) [12]. To address this issue, the describing function method can be used. This paper, however, only considers local absolute stability.

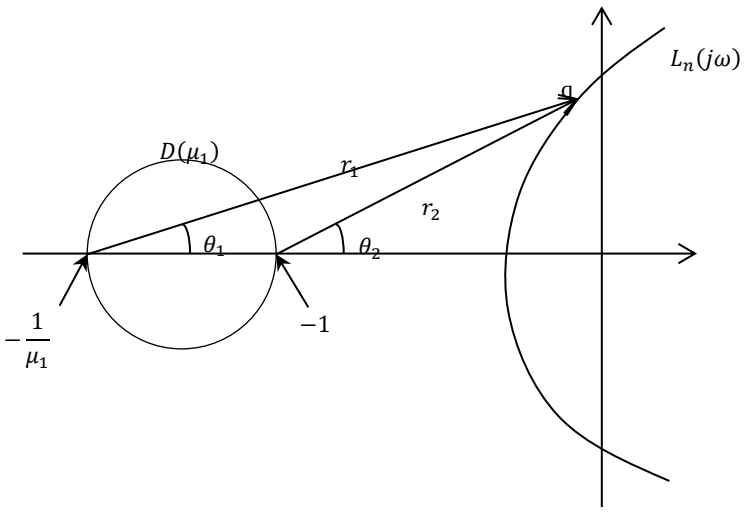

Fig. 2. Graphical representation of the circle criterion [11].

Since the other element affecting L_n, i.e., the linear loop transmission L, has already been determined; the focus now is on designing the compensator H such that L_n satisfies the circle criterion. By introducing the $\eta =$

$(1/\mu_1 + 1)/2$ and $\kappa = (1/\mu_1 - 1)/2$ and expressing L_n in terms of the real component "$\mathcal{R}$" and the imaginary component "$\mathcal{I}$", Eq. (5) may be reformulated as the following inequality.

$$\mathcal{I}_{L_n}^2 > \kappa^2 - \left(\mathcal{R}_{L_n} + \eta\right)^2 \tag{6}$$

Substituting of $\mathcal{R}_{L_n}$ and $\mathcal{I}_{L_n}$ from Eq. (1) and simplifying the resulting expression leads to inequality (7), which defines the admissible region for H in the Nyquist plane.

$$\begin{cases} \mathcal{I}_H > \mathcal{A}\mathcal{R}_H - \mathcal{B}; & \mathcal{I}_L > 0 \\ \mathcal{I}_H < \mathcal{A}\mathcal{R}_H - \mathcal{B}; & \mathcal{I}_L < 0 \end{cases} \tag{7}$$

where, $\mathcal{A} = -(1 + \mathcal{R}_L)/\mathcal{I}_L$ and $\mathcal{B} = -\left((1 + \mathcal{R}_L)(1 + \mu_1\,\mathcal{R}_L) + \mu_1\,\mathcal{I}_L^2\right)/\left(\mathcal{I}_L(1 - \mu_1)\right)$. The inequalities (7) are linear, and their parameters i.e., slope $\mathcal{A}$ and vertical intercept $\mathcal{B}$, are functions of linear loop transmission and μ_1. In plants with uncertainty, $\mathcal{A}$ and $\mathcal{B}$ may vary in certain ranges. Inequality (7) must be satisfied for all possible plant parameters. Each pair of plant parameters defines a line in the Nyquist plane, and the first and second inequalities of Eq. (7) correspond to the regions above and below the line $\mathcal{I}_H = \mathcal{A}\mathcal{R}_H - \mathcal{B}$, respectively. Fig. 3 illustrates the overall boundaries that express the constraint resulting from all possible plant parameters.

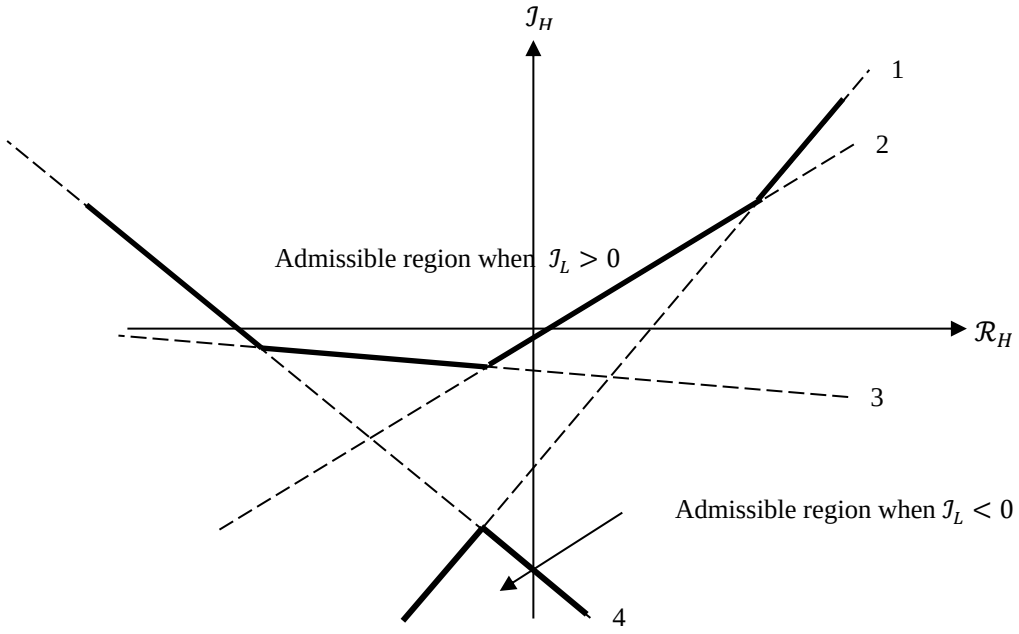

Fig. 3. Schematic representation of circle criterion constraint on H in Nyquist plane.

A common approach for compensator design in the QFT framework is to express the constraints in Nichols plane, simplifying the design process and making it more intuitive. Section 4, which is the main contribution of this paper, addresses the algorithm for mapping the constraints from Nyquist to Nichols plane.

3. ALGORITHM FOR MAPPING THE ADMISSIBLE REGION FROM THE NYQUIST TO THE NICHOLS PLANE

At first glance, the transformation of boundaries expressing the circle criterion constraint from the Nyquist plane to the Nichols plane may seem simple. However, as seen in the following paragraphs, this process has some details worth examining. Firstly, how can the overall boundary be calculated in the Nyquist plane?

3.1 Overall boundary determination in the Nyquist plane

To calculate the overall boundary that satisfies the circle criterion for all possible plant variants in the Nyquist plane, the process should start from one end of the overall boundary schematically shown in Fig. 3. Here; the left side is selected. The upper boundary begins with the steepest lines at both ends, with the most negative slope on the left and the most positive slope on the right. If the lower boundary is applicable, the signs of slopes are switched.

The algorithm starts with the sorting of slope and vertical intercept of lines in two separate row vectors

$\boldsymbol{A} = \{a_i\}_{1\times n_l}$ and $\boldsymbol{B} = \{b_j\}_{1\times n_l}$, respectively, with descending/ascending order based on upper/lower boundary slopes. Here, n_l is the number of plant variants. Next, two matrices are defined as $\boldsymbol{X} = [\infty]_{n_l\times n_l}$ and $\boldsymbol{Y} = [0]_{n_l\times n_l}$ as initial values of abscissa and ordinate of all intercepts of each line pair, these matrices will be filled with true values according to Eq. (8).

$$\begin{cases} x_{ij} = -(b_i - b_j)/(a_i - a_j) \\ y_{ij} = a_i x_{ij} + b_i \end{cases} \quad ; \quad i \neq j \tag{8}$$

Sorting the lines based on their slopes, the pair of first columns of matrices X and Y contain the intercepting points of the line with the most negative slope/most positive slope with other lines. Referring to Fig. 3, starting from $x = -\infty$ and sliding along the steepest applicable line draws the first part of the overall boundary up to the first intercepting point. The coordinate of this point is expressed by the smallest element of the first column of X and its corresponding pair in the matrix Y with the same position (i_1, j_1). The next line on the overall boundary is the one that creates the first intercept in conjunction with the line of the most negative slope. Hence, the second line on the border corresponds to i_1th column in matrices X and Y. Sliding along this line up to the next intercept. The abscissa of this point is expressed by the smallest element of the column i_1th of matrix X, which is larger than $X(i_1, j_1)$. Its ordinate is the corresponding pair in matrix Y with the same position (i_2, j_2). This process is continued until reaching the line with the most positive slope/ most negative slope and sliding along it to $x = +\infty$.

3.2 Mapping a line from the Nyquist plane onto the Nichols plane

As explained initially, Nichol's chart facilitates compensator design, especially in the QFT framework. Therefore, the transformation of the borders from the Nyquist plane to the Nichols plane is discussed here. As observed, the overall boundary of the circle criterion in the Nyquist plane is a piecewise linear function. Therefore, the first step in mapping is to understand the projection of a line from the Nyquist plane to Nichol's plane. The projection of a general line from the Nyquist plane to the Nichols plane is a U-shaped curve with an aperture of 180°. Its deepest point's ordinate is equal to the distance of the line from the origin of the Nyquist plane on dB scale. The axis of symmetry of the curve lies at an angular position that is identical to the angle of the normal to the line from the origin of the Nyquist plane concerning the real axis. Phase angle in Nichols plane usually spreads in the domain of $-360° \le \phi \le 0$ or $-180° \le \phi \le 180°$. By definition, absolute gain or modulus ρ is assumed to be positive. Taking a left-hand side plot in Fig. 4 as an example (a1), when a radial beam sweeps the Nyquist plane from $\phi = -360°$, there is no intercept with a boundary line up to $\varphi = -2\pi + \tan^{-1} a$ where a is the slope of the boundary line.

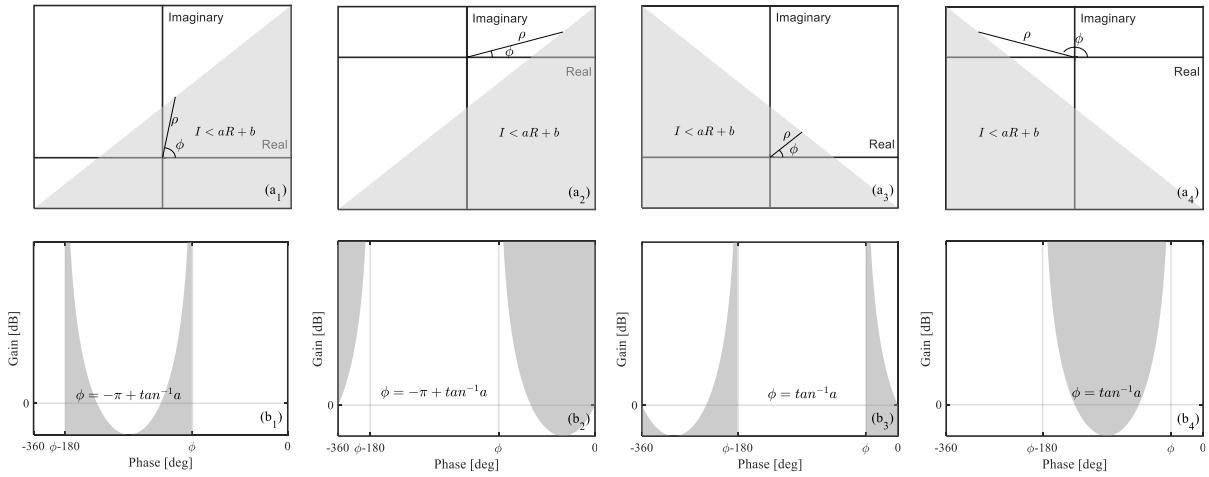

Fig. 4. Graphical representation of the mapping of a region specified by a line from the Nyquist plane to the Nichols plane for $\mathcal{I}_L < 0$.

From φ up to $\varphi + 180°$, the modulus reduces from $+\infty$ to a minimum value as described above and then increases back up to $+\infty$. This mapping is presented in the right-hand side plots of Fig. 4, for example, (b1). Therefore, in the Nichols plane, some part of the phase axis corresponding to negative modulus values will not contribute to the domain of the mapped boundary.

Depending on the sign of the slope and vertical intercept of the boundary line in the Nyquist plane, the mapped boundary in the Nichols plane shifts along the phase axis. The first row of Fig. 4 corresponds to the boundary line with positive slope and positive vertical intercept. The subsequent rows are associated with the other slope and vertical intercept sign combinations. In

these cases, mapping the boundary line from the Nyquist plane to the boundary curve in the Nichols plane can be explained as it was done for the first row. When the boundary line passes through the origin of the Nyquist plane, its projection onto the Nichols plane is a vertical line at the phase angle of $\tan^{-1} a$.

3.3 Mapping the admissible region from the Nyquist plane onto the Nichols plane

After mapping the boundary line from the Nyquist plane to the Nichols plane, the gray region above/below it that is admissible for H as imposed by the first/second part of the condition (7), associated with the linear loop transmission with a positive/negative imaginary part i.e., $\mathcal{I}_L > 0$ / $\mathcal{I}_L < 0$ should be determined on the Nichols plane. When $\mathcal{I}_L < 0$, as seen in the first row of Fig. 4, for H to be in the gray region of the plot (a1), the absolute magnitude of H should be smaller than ρ. Therefore, the admissible region for $\|H\| \triangleq 20 \log |H|$ will be below the boundary curve in the Nichols plane, as shown in plot (b1). With a positive slope and negative vertical intercept, $|H| \geq \rho$ is required for H to be in the gray region of the plot (a2), and consequently, the admissible region is above the boundary curve. Plot (b2) shows this region. The third and fourth rows of Fig. 4 can be explained similarly. When, $\mathcal{I}_L > 0$, a similar explanation is applicable.

3.4 Flowchart representation of the circle criterion implementation algorithm

This section considers the algorithm for implementing the abovementioned process, using flowcharts to provide a straightforward guide for writing computer codes. The linear design phase leads to the loop transmission $L(j\omega)$, which, for the domain of variations of system parameters in a desired frequency range, constructs a $n_\omega \times n_l$ matrix, where n_ω is the number of design frequency points. According to formulation in section 3, this matrix, together with μ_1, which is the lower limit of section nonlinearity saturation, are the inputs of the algorithm. The first step of the algorithm prepares the slope and vertical intercept of all boundary lines related to all possible plant variants the designer considers. At this step, the vectors of slopes and vertical intercepts are sorted in descending/ascending order based on the slopes vector, according to the applicability of the first/second inequalities in Eq. (7), as shown in Fig. 5.

In the next step, finding all the intersecting points is shown in the flowchart in Fig. 6. Sorted vectors of slopes and vertical intercepts are the inputs to this algorithm step. The abscissa and ordinate of intersecting points are gathered in two $n_l \times n_l$ matrices $\boldsymbol{X}$ and $\boldsymbol{Y}$, respectively. The element in the position of the ith row and jth column of these matrices indicates the coordinate of the intersecting point of line ith and line jth. The main diagonal elements are set at the right end of the real axis. A schematic representation of matrix $\boldsymbol{X}$ is shown in Fig. 7.

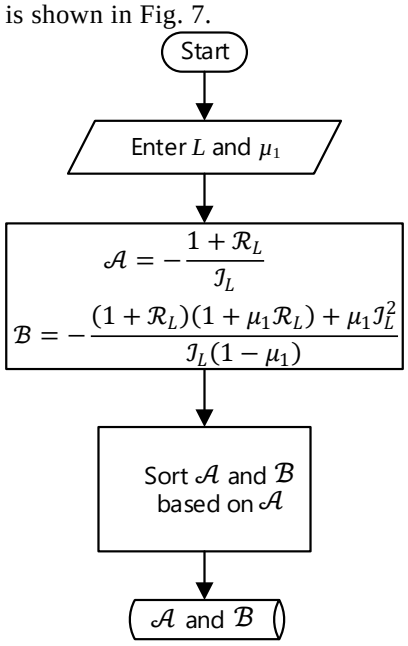

Fig. 5. Flowchart for preparing sorted vectors of the slopes and. vertical intercepts.

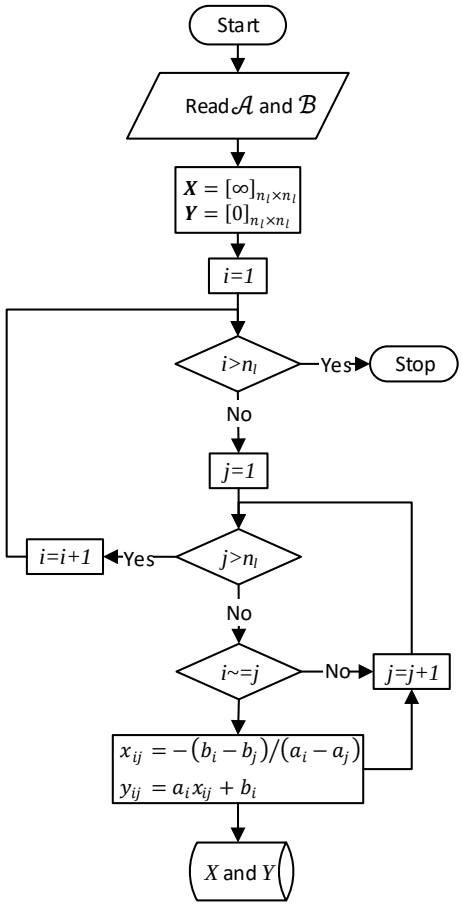

Fig. 6. Flowchart for finding all the intercept points.

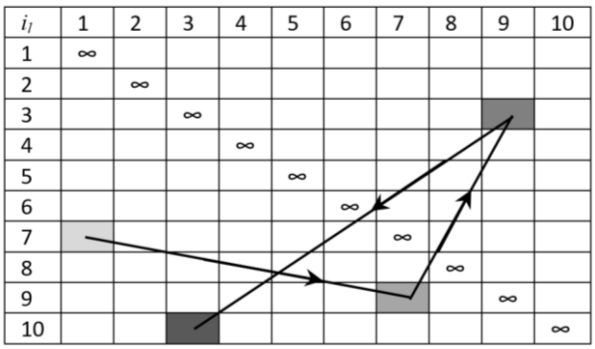

Fig. 7. Graphical representation of finding intersecting points on the overall boundary using matrix ***X*.**

The flowchart in Fig. 8 can be used to find intersection points on the overall boundary. From the left of the Nyquist plane, the most negative slope/most positive slope line begins the overall boundary. The first column of matrix ***X*** in Fig. 7 corresponds to this line. Sliding along this line up to the first intercept is associated with the smallest column element. This element is indicated by the lightest gray color in Fig. 7. The row number of this element is associated with the index of the next line, constructing the overall boundary. For the example shown in Fig. 7, row 7 is associated with the first intersection; consequently, line 7, represented by column 7, is the second constructing line of the overall boundary.

Again, sliding along this line leads to the next intersecting point on the overall boundary, shown by a slightly darker gray cell than the previous cell in schematic Fig. 7. The abscissa of this point is the smallest element of this column that is greater than the abscissa of the previous point. To satisfy this condition, the previous point's abscissa is subtracted from all elements of the recent column. Therefore, the row number of the smallest positive element in the changed-pivot column is associated with the index of the next line on the overall boundary. This process continues until the line with the most positive/negative slope is reached, as shown graphically in Fig. 7 using arrows and gradually darkening cells in the schematic representation of matrix ***X***. Fig. 8 can be used to develop the computer code.

At the end of this step, the coordinates of breakpoints on the overall boundary and the index of lines on this boundary are available. Provide the coordinate of the breaking points, the line with the most negative slope/most positive slope, and the line with the most positive slope/ most negative slope at the left and right of the overall boundary, entrance, and exit angles to and from each part of the boundary between two successive breaking point or entrance and exit angles to or from most right or most left part of the overall boundary can be calculated. The flowchart presented in Fig. 9 illustrates this process.

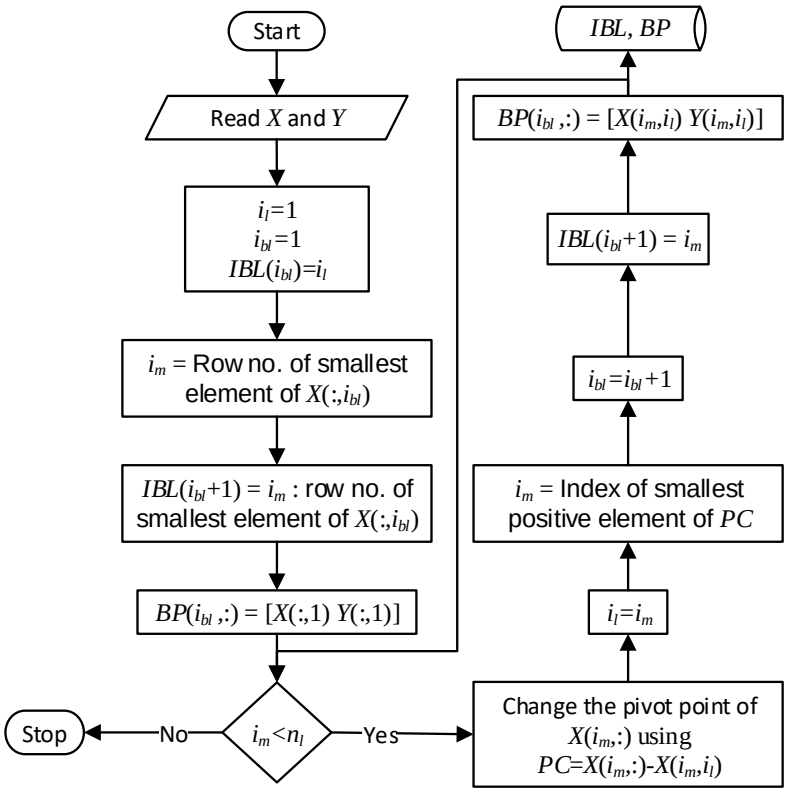

Fig. 8. Flowchart for finding intersecting points on the overall boundary using matrix ***X*.**

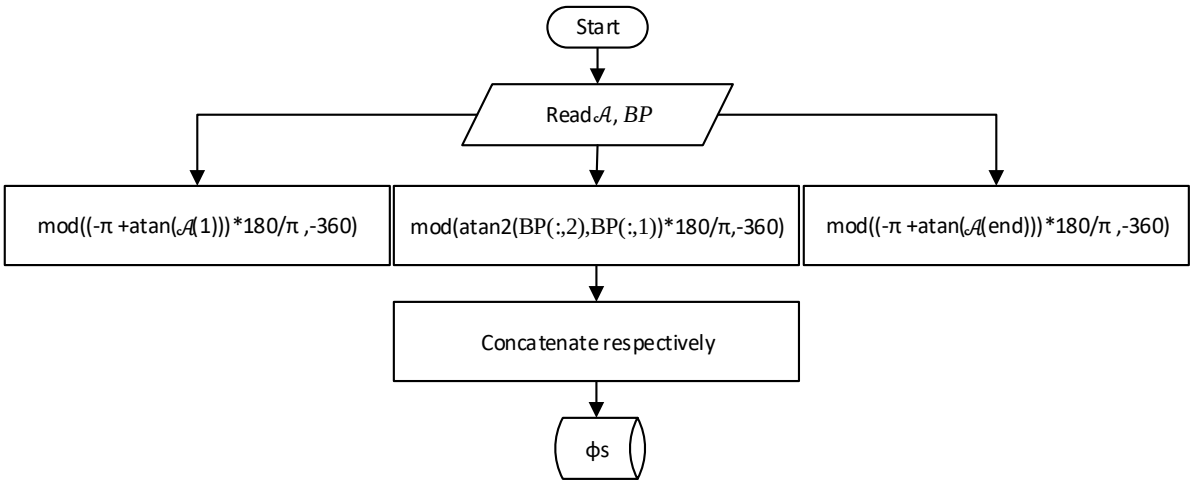

Fig. 9. Flowchart for calculating the entrance and exit angles to and from each part of the overall boundary.

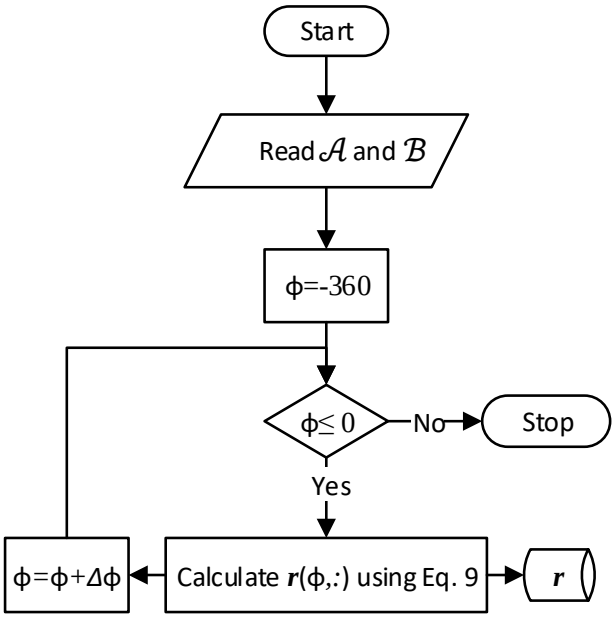

Fig. 10. Flowchart for calculating the gain associated with the lines that contribute to the overall boundary in the absolute scale.

The variable BP contains the coordinates of the breakpoints. The flowcharts in this paper use MATLAB functions and notations for brevity. The command "$\mathrm{mod}(\theta, -360)$" maps any angle θ in the range of $[-360°, 0°]$. The command "$\theta = \mathrm{atan}(y/x)$" calculates $\theta \in [-\pi/2, \pi/2]$ and the command "$\theta = \mathrm{atan2}(y, x)$" calculates $\theta \in [-\pi, \pi]$.

Up to this point, the required data for transferring the overall boundary from the Nyquist plane to the Nichols plane has been calculated. The final step is dedicated to the transformation. In this step, after transforming the boundary, it will be determined which side of the boundary is admissible for designing compensator H.

By sweeping a radial beam in the Nyquist plane from $-360°$ to $0°$, when it intersects with the overall boundary, the upper or lower limit of $|H|$, i.e., ρ, is equal to the length of the beam that can be calculated as follows.

$$\rho = \frac{\mathcal{B}(IBL)}{\sin \Phi - \mathcal{A}(IBL) \cos \Phi} \tag{9}$$

Here, Φ is the phase vector in the domain of $[-360°, 0°]$ with a desired interval of $\Delta\phi$ and $\phi \in \Phi$ in the flowchart of Fig. 10 that calculates the modulus associated with the lines contributing to the overall boundary at each phase angle ϕ. IBL is a vector that contains the indices of the lines contributing to the construction of the overall boundary.

Now, noncontributing parts of each line must be eliminated from the overall boundary in the Nichols plane. To achieve this, eight different conditions should be considered, as shown in Fig. 11. As seen in this figure, from the left-hand side, the first and third situations in the first row and the second situation in the second row have an interesting range of phase angle determined by inequalities in the reverse direction of other situations.

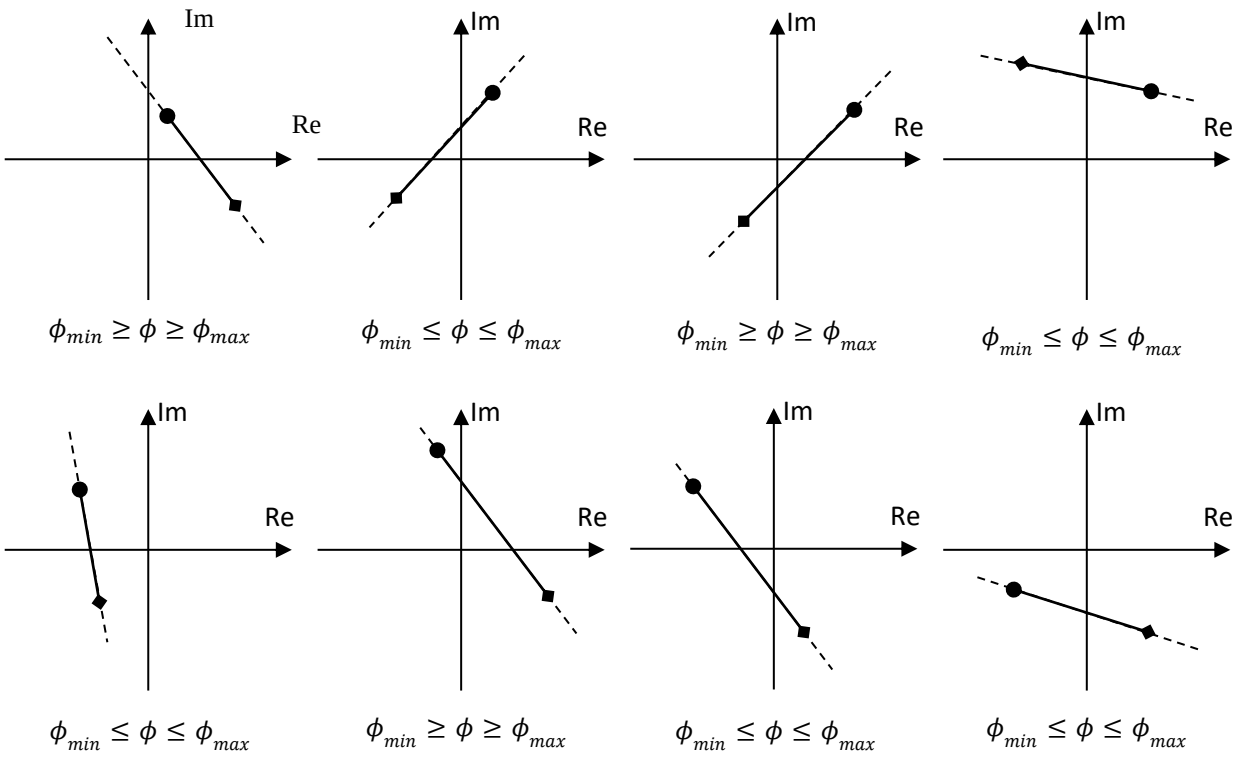

Fig. 11. Angle range of interest in the various conditions of vertical intercept and entrance and exit angles, ϕ_min and ϕ_m ax denoted by • and ■, respectively.

According to the above discussion, the flowchart in Fig. 12 provides the overall boundary of the admissible modulus of $H(j\omega)$ in the dB scale for the angle range of interest. In this flowchart, n_L is the number of lines that contribute to constructing the overall boundary, and ϕs is provided by the flowchart in Fig. 9. Here, NaN (i.e., not a number) is borrowed from Matlab software.

The final stage of the process is determining which side of the overall boundary is admissible. According to Eq.(7), if the linear loop transmission, which is the result of the first design step, has an imaginary part that satisfies $\mathcal{J}_L < 0$ by returning to Fig. 4, the admissible value for $H(j\omega)$ in the Nichols plane is $|H(j\omega)| \leq \rho$ if the vertical intercept of the associated line in the Nyquist plane is positive and vice versa. On the contrary, if the resultant loop transmission from the first design step has an imaginary part that satisfies $\mathcal{J}_L > 0$ by returning to Fig. 4, the admissible value for $H(j\omega)$ in the Nichols plane is $|H(j\omega)| \geq \rho$ if the vertical intercept of the associated line in the Nyquist plane is positive and vice versa.

After describing the algorithm, an example is solved, and its results are presented step by step to illustrate the process and validate the algorithm.

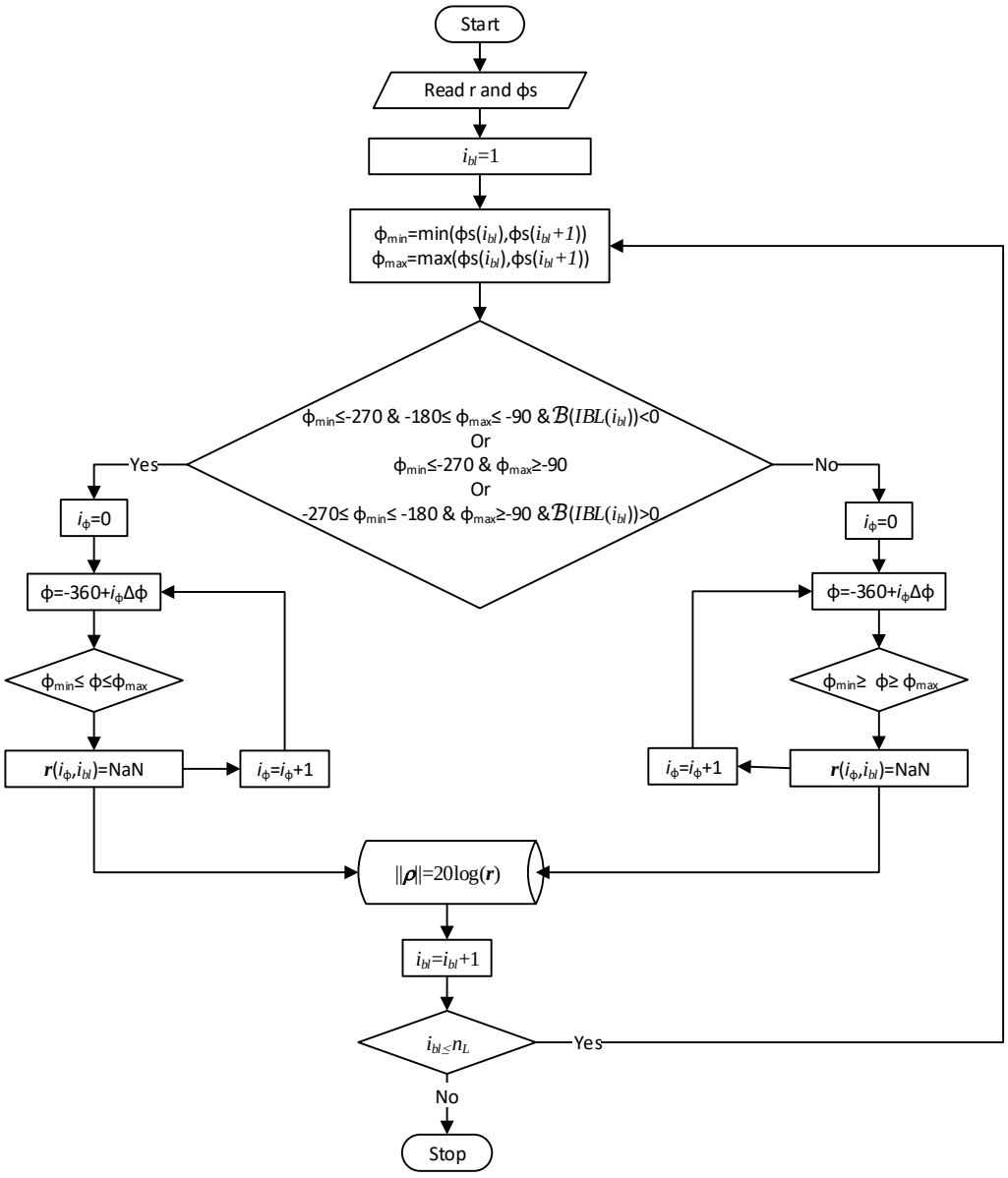

Fig. 12. Finalizing the boundary of the admissible modulus of $H(j\omega)$ for representation in the Nichols plane.

4. EXAMPLE AND ALGORITHM VERIFICATION

A wide variety of actuators, such as electromechanical, electromagnetic, and electrohydraulic types, are used is space applications. To examine the validity of the proposed algorithm, an electrohydraulic actuator is considered here. The transfer function of a hydraulic actuator, given by Eq. (10), is a customized form employed in [13], with inertial terms ignored and some differences in the numerical values of parameters. This transfer function, with actuator force as the output and the excitation voltage as the input, is used for the algorithm verification process. Saturation reflects itself in this plant as the limitation of the excitation voltage to 24 v.

$$P = \frac{K_s(A_i + A_o)}{R} \frac{(d + d_e)s + k_e}{D_3 s^3 + D_2 s^2 + D_1 s + D_0} \tag{10}$$

where,

$$\begin{aligned} D_0 &= K_p k_e \\ D_1 &= A_i^2 + A_o^2 + K_p(d + d_e) + Ck_e + k_e K_p \tau \\ D_2 &= \left(A_i^2 + A_o^2\right)\tau + \left(C + K_p \tau\right)(d + d_e) + Ck_e \tau \\ D_3 &= C(d + d_e)\tau \end{aligned} \tag{11}$$

and $A_i = 855\ mm^2$, $A_o = 428\ mm^2$, $d = 200\ Ns/m^2$, $d_e = 100\ Ns/m^2$ and R=28 Ω represente the piston's extending side area, retracting the piston, retracting side area of the piston, damping coefficient of cylinder-piston contact region, damping coefficient of load and electrical resistance of proportional valve solenoid, respectively. The other parameters vary in the range listed in Table 1.

Table 1. Nominal value and variation range of the plant parameters**.**

Parameter	Description	Nominal value	Range
k_e	Load stiffness	$5 \times 10^5 [N/m]$	[267,985000]
K_i	Flow rate sensitivity to excitation current	$1.5 \times 10^{-3} [m^3/As]$	$[1,2] \times 10^{-3}$
K_p	Flow rate sensitivity to pressure difference	$-65 \times 10^{-12}\ [m^2/sPa]$	$[-65,2650] \times 10^{-12}$
C	Flow rate sensitivity to pressure rate	10.7×10^{-15}	$[8.56,12.83] \times 10^{-15}$
τ	Solenoid time constant	$22.5\ ms$	[20,25]

As the first stage of the design process, the nominal values listed in this table are used to shape the loop using the QFT method, which results in the following transfer function for the loop transmission $L_0 = GP_0$. Details of this design stage are not presented for brevity, and readers can refer to [13] for more information.

$$L_0 = 10^7 \frac{7.2s^3+6.7\times10^2 s^2+1.7\times10^4 s+4.4\times10^4}{s^5+4\times10^4 s^4+10^6 s^3+2.6\times10^7 s^2+1.3\times10^7 s} \quad (12)$$

The degrees of the numerator and denominator of L are the same as those as L_0, but their coefficients vary depending on changes in the plant parameters. Assuming only the lower and upper limits of parameter variations listed in Table 1, there are 32 possible plant variants. H must be designed to satisfy the circle criterion for all variants. To examine the algorithm, $L_{n_\omega \times n_l}(j\omega)$ and $\mu_1 = 0.001$ are used in this example. By implementing the flowcharts shown in Fig. 5, Fig. 6, and Fig. 8 for frequencies $\omega = 0.1\ rad/s$, $\omega = 50\ rad/s$ and $\omega = 600\ rad/s$, boundaries related to each variant of the plant are obtained. These boundaries are shown as dotted lines in Fig. 13. To ensure that the circle criterion is satisfied for all plant variants, H must be designed accordingly.

The solid lines in the first row of Fig. 13 represent the overall boundary that satisfies this condition, while the downward-filled triangles along the border indicate the region of admissibility. The Nyquist plane data for the boundary is used as input for the flowcharts shown in Fig. 9, Fig. 10, and Fig. 12 to obtain the admissible region in the Nichols plane. The outputs, i.e., the boundaries on $|H|dB \triangleq \|H\|$ (represented by CCB), are presented in the second row of Fig. 13, with lower and upper limits indicated by black and gray colors, respectively.

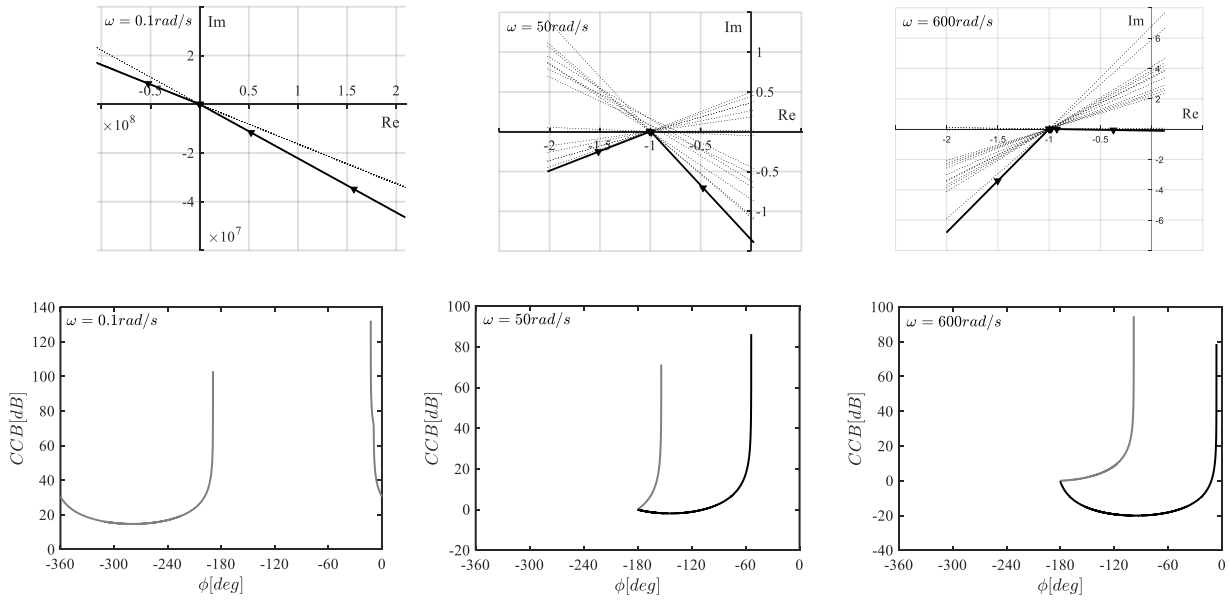

Fig. 13. Circle criterion boundaries for 3 selected frequencies, top plots: Nyquist representation, bottom plots: Nichols representation.

If $H(j\omega)$ is designed to fall within the admissible region of the Nyquist or Nichols planes, as shown in Fig. 13, then loop transmission around the saturation element, $L_n(j\omega)$, will not penetrate the circle centered at $(-(-1-1/\mu_1)/2\,,0)$ with a radius $(-1+1/\mu_1)/2$ in the Nyquist plane.

For validation, breaking points of the overall boundary in the Nyquist plane are selected as testing points and employed to generate associated points on $L_n(j\omega)$ according to Eq. (1). For all variants of plant at 16 frequencies in the band $0.1\ rad/s \le \omega \le 600\ rad/s$, $L_n(j\omega)$ scatters in the Nyquist plane, as shown in Fig. 14. In part (a) of this figure, all points associated with all plant variants at 16 frequencies are presented. However, due to scale inconsistency, the circle of criterion is not visible in this part of the figure. Part (b) of this figure presents a magnified view of part (a) in the vicinity of the circle of criterion. As seen, there is no scattering of points in the region within the circle of criterion. This region is considered the forbidden region because the transfer function of the closed-loop system becomes unstable if the loop transmission around the saturation element penetrates this region. The absence of scattering in the forbidden region indicates that the algorithm properly calculates the overall boundaries.

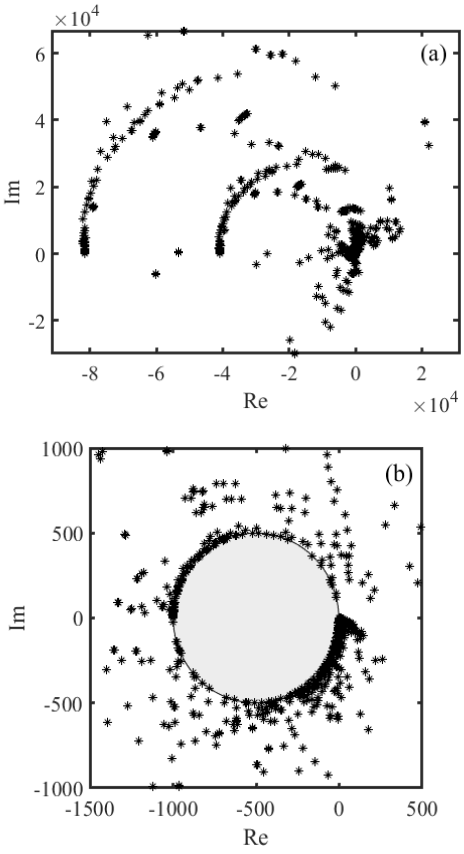

Fig. 14. Examining the algorithm by direct check using the circle of criterion in the Nyquist plane.

5. CONCLUSION

QFT is a powerful, robust tool for designing controllers in the presence of plant uncertainty and input saturation, which are prevalent in space systems and components. One approach to achieve this is using noninterfering architecture, where a robust linear controller is first designed through loop shaping and prefiltering, ignoring saturation. Then, a loop is constructed around the saturation element to mitigate its undesired effects, and robust stability depends on satisfying the circle criterion.

However, the computational cost of calculating the boundaries of the circle criterion makes automation necessary. This paper provides a detailed algorithm for implementing the circle criterion in practice, using flowcharts to facilitate computer code generation.

An example demonstrates the algorithm, with intermediate and final results provided to track the process. Finally, direct validation confirms that the calculated overall boundary satisfies the circle criterion.

CONFLICT OF INTERESTS

No conflict of interest has been expressed by the author.

REFERENCES

[1] C. Wen Hua, "QFT design for spacecraft with uncertain flexible structures," in *6th World Congress on Intelligent Control and Automation*, Dalian, China, 2006, pp. 8191-8195, https://doi.org/10.1109/WCICA.2006.1713571.

[2] M. V. Chitra, K. K. Sharma, and A. A. Kumar, "Quantitative feedback theory based robust control design for a flexible luanch vehicle," in *International Conference on Control, Communication, and Computing India (ICCC)*, Trivandrum, India, 2015, pp. 72-77, https://doi.org/10.1109/ICCC.2015.7432872.

[3] M. Garcia-Sanz, I. Eguinoa, M. Barreras, and S. Bennani, "Nondiagonal MIMO QFT controller design for Darwin-type spacecraft with large flimsy appendages," *Journal of Dynamic Systems, Measurement, and Control*, vol. 130, no. 1, 2008, Art. no. 011006, https://doi.org/10.1115/1.2807067.

[4] C. H. Houpis, S. J. Rasmussen, and M. Garcia-Sanz, *Quantitative Feedback Theory: Fundamentals and Applications*, 1st ed. Boca Raton, FL, USA: CRC Press, 1999, https://doi.org/10.4324/9780203908051.

[5] W. Wu and S. Jayasuriya, "A new QFT design methodology for feedback systems under input saturation," *Journal of Dynamic Systems, Measurement, and Control*, vol. 123, no. 2, pp. 225-232, 1999, https://doi.org/10.1115/1.1367337.

[6] "Control System Toolbox," MathWorks, R2013a, 2013.

[7] C. Borghesani, Y. Chait, and O. Yaniv, *The QFT frequency domain control design toolbox*, 3rd ed. San diego, CA: Terasoft, Inc., 2003.

[8] M. García Sanz and J. A. Osés, "Evolutionary algorithms for automatic tuning of QFT controllers," in *23rd IASTED International Conference Modelling, Identification and Control*, Grindelwald, Switzerland, 2004, Art. no. 412-094.

[9] I. Horowitz, "A synthesis theory for a class of saturating systems," *International Journal of Control*, vol. 38, no. 1, pp. 169-187, 1983, https://doi.org/10.1080/00207178308933067.

[10] W. Wu, and S. Jayasuriya, "Controller design for a nonovershooting step response with saturating nonlinearities," in *American Control Conference (Cat. No. 99CH36251)*, San Diego, CA, USA, 1999, pp. 3046-3050, https://doi.org/10.1109/ACC.1999.782321.

[11] H. Khalil, "Frequency domain analysis of feedback systems," in *Nonlinear Systems*, Prentice Hall, 2002, pp. 263-279.

[12] W. Wu and S. Jayasuriya. "Design of feedback systems with plant input rate saturation via QFT approach," *Journal of Dynamic Systems, Measurement, and Control*, vol. 128, no. 3, pp. 701-705, 2006, https://doi.org/10.1115/1.2232693.

[13] N. Niksefat and N. Sepehri, "Design and experimental evaluation of a robust force controller for an electro-hydraulic actuator via quantitative feedback theory," *Control Engineering Practice*, vol. 8, no. 12, pp. 1335-1345, 2000, https://doi.org/10.1016/S0967-0661(00)00075-7.